IEEE TRANSACTIONS ON NUCLEAR SCIENCE, VOL. 43, NO. 3, JUNE 1996, PP. 1952-1957

Initial Results from the Sherbrooke Avalanche Photodiode Positron Tomograph

R. Lecomte, J. Cadorette, S. Rodrigue, D. Lapointe,
D. Rouleau, M. Bentourkia, R. Yao and P. Msaki
Department of Nuclear Medicine and Radiobiology,
University of Sherbrooke, Sherbrooke (Québec), Canada J1H 5N4

Abstract

The design features and engineering constraints of a PET system based on avalanche photodiode (APD) detectors have been described in a previous report. In this paper, we present the initial results obtained with the Sherbrooke APD-PET scanner, a very high spatial resolution device designed for dynamic imaging of small and medium-sized laboratory animals such as rats, cats, rabbits and small monkeys. Its physical performance has been evaluated in terms of resolution, sensitivity, count rate, random and scatter fractions, contrast and relative activity recovery as a function of object size. The capabilities of the scanner for biomedical research applications have been demonstrated using phantom and animal studies.

I. Introduction

The potential of the PET approach to study *in vivo* tracer pharmacokinetics and metabolism [1-6] has triggered an interest in the development of a number of specialized small animal PET systems [7-12]. The most stringent requirement for small animal imaging by PET is spatial resolution. Whilst the resolution of 3-4 mm FWHM currently achievable with existing PET systems [6-9,13] is sufficient for resolving gross anatomical structures and measure dynamic changes in medium-sized animals, it is inadequate for regional quantitation of tracers in small animals (rats, mice, etc.) due to partial volume effects.

The first PET scanner based on avalanche photodiode (APD) detectors which has recently entered into operation at University of Sherbrooke was designed to resolve this difficulty by using small discrete detectors and parallel signal processing. With such a design, the system achieves a spatial resolution of nearly 2 mm FWHM. The scanner has a 12 cm diameter useful field-of-view (FOV), making it ideal for dynamic imaging of small and medium-sized laboratory animals. At its present stage of development, the scanner consists of a single 10.5 mm thick layer of detectors which enabled the initial characterization of its physical performance.

II. System Description

The design characteristics and engineering constraints of the scanner have been described previously [14]. Its main physical characteristics are summarized in Table I. In short, the initial system consists of 256 BGO-APD dual detector modules grouped into 32 single-layer cassettes. The signals from each detector are processed in parallel to generate timing and digitized energy signals which are concentrated and routed to 12 coincidence units. On-time and off-time coincidence data are sorted out and recorded in histogram mode using programmable data selectors interfaced to three RISC processors. The acquisition hardware and all system controls interface directly to a PC-386 computer operating under DOS/Windows.

As APD detector tuning is critical for good timing performance, high-voltage bias and all set-up parameters are adjusted under computer control for each individual detector [15]. Steady temperature at the detector site is maintained by thermoelectric cooling. The "clam-shell" motion [16] was used to provide the required sampling density. Without sampling motion, the set of parallel lines-of-response (LOR) between opposing groups of detectors defines a projection of 64 1.9 mm wide bins. With the clam sampling, the data are rebinned into 128-bin projections at an average 0.95 mm interval. The system also implements a stepper motor driven rotating source with a remote pneumatic actuator used for normalization of the detector efficiency and for acquiring the transmission scans required for attenuation correction. A bed with manual vertical adjustment and computer-controlled horizontal positioning has recently been added.

Table I

Description of the Sherbrooke animal PET scanner

Detector type	EG&G model C30994
Number of detectors	512 (256 / ring)
BGO crystal size	3 x 5 x 20 mm (beveled)
Module dimension	3.8 x 13.2 x 33 mm
BGO crystal spacing	3.8 mm in-plane 5.5 mm axially
Detector rings	2 (1 layer of modules)
Ring diameter	310 mm
Port diameter	135 mm
Useful field-of-view	118 mm
Axial field-of-view	10.5 mm
Reconstruction planes	3 (2 direct, 1 cross)
Plane interval	2.75 mm
Sampling	Clam-shell, 2 positions
Number of LORs	98,304 (total) / 65,536 (useful)

III. PERFORMANCE EVALUATION

The set of performance evaluation measurements carried out for this animal scanner was inspired and adapted from the guidelines proposed by the SNM/NEMA test protocol [17]. The performance phantom used in this study was a straight-side polycarbonate jar (Nalgene) with an internal diameter of 108 mm and a wall thickness of 1 mm. As the ring assembly can be tilted horizontally, the phantom was imaged in the upright position. A 0.84 mm active diameter line source of ^{22}Na (177 μCi/cm) sheathed in a 1.24 mm O.D. steel tubing was used for the resolution, scatter and absolute efficiency measurements. All measurements were made with an energy discrimination of 350-700 keV set individually on each detector and a coincidence time window of 25 ns. The noise threshold of individual detectors was adjusted to limit the noise rate to a maximum of 3 kcps in the front-end electronics thereby limiting the contribution of electronic noise to coincidence deadtime to less than 3% [15].

Images were reconstructed by filtered backprojection on a 128×128 grid with a pixel size of 0.95 mm, using a ramp filter with 0.53 mm^{-1} cut-off frequency. Data obtained without sampling motion were interpolated to 128-bin projections before reconstruction.

A. Spatial Resolution

The transaxial spatial resolution was measured at every 5 mm from center to a radial position of 55 mm using the ^{22}Na line source positioned axially in the FOV. Measurements were obtained with and without the clam sampling motion. With clam sampling, measurements were repeated in both the parallel and perpendicular directions relative to clam motion and averaged out. Radial and tangential profiles through the center of the reconstructed images were least-square fitted as Gaussian functions to match the FWHM and FWTM values.

The axial slice profile width was determined by stepping the ^{22}Na line source in 0.35 mm increments through the axial FOV at several radial positions in the field. The axial profiles were analyzed for diametrically opposite groups of detectors and the FWHM and FWTM determined for the direct and cross planes by linear interpolation.

B. Sensitivity

The sensitivity of the scanner in air was measured using the line source of ^{22}Na placed axially at the center of the FOV. The absolute efficiency to a point source was estimated from this measurement by averaging using the axial slice profiles. The system sensitivity was determined from the count rate response of the scanner (see below) to a low concentration (< 3 μCi/ml) uniform distribution of activity.

C. Count Rate

The count rate characteristics were measured using the performance phantom loaded with 135 ml of a solution of ^{18}F. With this volume, about 26% of the activity was outside the field when the phantom was centered in the FOV. As other studies were conducted concurrently with the count rate measurements, data were collected in 150-200 second frames at irregular intervals over 9 half-lives. The initial radioactivity concentration was 132 μCi/ml. This was merely sufficient to reach the 50% deadtime point, but neither the trues saturation count rate nor the point at which the trues and randoms rates are equal was attained. The system deadtime was estimated by extrapolating the ideal trues count rate from the low activity concentration data. The noise equivalent count rate (NEC) was calculated from the recorded trues and randoms count rate data and from the object scatter fraction estimated as described in the following section. A noiseless estimate of the randoms was assumed, since the statistical noise in the recorded sinograms of the delayed randoms can be filtered before correction. The high count rate response of the tomograph was also evaluated with a total activity of 20 mCi in 1 ml centered in the FOV.

D. Scatter

The fractions of object and detector scatter were estimated from a single tomographic measurement taken with the ^{22}Na line source placed at 50 mm from the center of a plexiglas cylinder of diameter 110 mm and 25.4 mm thick using the methods proposed by Bentourkia et al. [18].

E. Image Quality

The investigation of the scanner imaging performance was based on phantom and small animal studies. A 11 cm diameter hot/cold spot phantom with spot diameters of 2, 3.4, 6.7, 9.7, 13, 15.8, 20.3 and 22.7 mm was used to estimate the quantitation capability of the system. Images were acquired for 30 minutes using the same water solution of ^{22}Na having a concentration of 12 μCi/ml. The contrast was evaluated as:

$$C(\%) = 100 * \frac{H - C}{H}$$

where H and C are the count densities in hot and cold regions, respectively. Relative recovery factors were calculated as:

$$RF(\%) = 100 * \frac{N - B}{N_{max} - B}$$

where N is the count density within the spot, B is the background and N_{max} is the count density in the largest spot.

To illustrate the imaging ability of the scanner for biomedical research applications, a preliminary animal study was performed with ^{18}F-fluoride ion, a bone-seeking tracer. Dynamic images of a section through the thorax of an anesthetized 160 g rat were acquired for 27 minutes (7×60 s and 4×120 s frames) following intraperitoneal administration of 626 μCi of ^{18}F-fluoride. Regional time activity curves were obtained of the tracer uptake in bones, the cardiac blood pool and soft tissue. Static image frames of 3 minutes (at the beginning of the scan) were then collected over the whole body of the rat at 8.25 mm intervals to obtain a uniform axial sampling of 2.75 mm. X-ray CT images of the same animal were subsequently taken with the same slice spacing for matching anatomical and functional images.

IV. RESULTS

A. Spatial Resolution

Spatial resolution data measured in the reconstructed images and in the axial direction are summarized in Figs. 1 and 2. A significant difference is observed between the resolution measured in stationary mode and with sampling motion. This is due to the poor packing fraction of the detectors in-plane (79%) which makes over sampling necessary to reach the intrinsic detector resolution. With clam sampling, the resolution at the center is 2.1 mm FWHM (4.0 mm FWTM) in the direction parallel to the clam motion and 2.2 mm FWHM (4.2 mm FWTM) in the direction perpendicular to the clam motion. At 1 cm from the center, the resolution is 2.4 mm FWHM (4.4 mm FWTM). This is slightly worse than the resolution previously measured using a rotation-translation sampling scheme [14] due to uneven sampling along the two axis with the clam motion. Regardless of this, the resolution is still very uniform up to 3 cm from the center and the degradation is only moderate in the radial direction as the source is moved further away.

The axial resolution on average is 3.1 mm FWHM (5.5 mm FWTM) at the center of the ring and it remains below 4 mm FWHM almost up to the edge of the useful FOV.

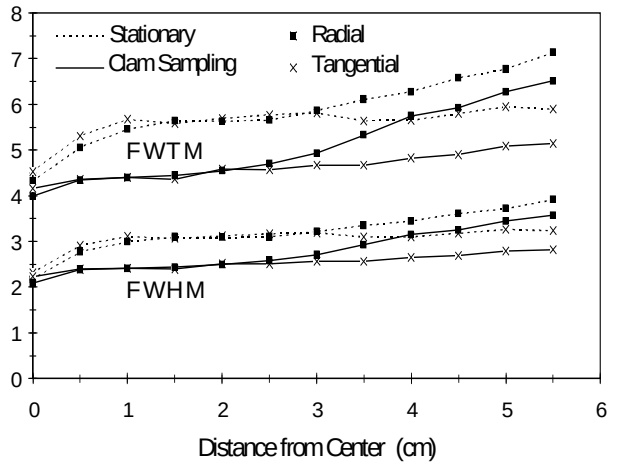

Fig. 1 - Radial and tangential resolution in the reconstructed image as a function of distance from center.

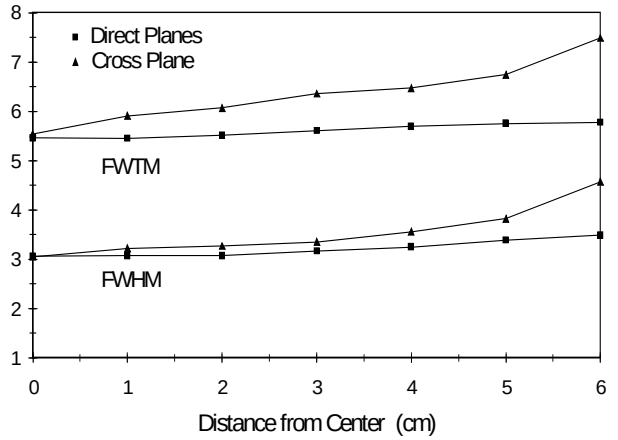

Fig. 2 - Axial resolution as a function of radial distance from the center measured by stepping the line source between diametrically opposite detectors.

B. Sensitivity

The sensitivity data after random correction for the line source and after random and scatter corrections for the uniform source distribution are summarized in Table II. The scanner absolute efficiency is estimated to be 0.51%.

Table II
Sensitivity data for the Sherbrooke animal PET scanner*

Axial line source in air at center of FOV		
	(cps/mCi/cm)	(cps/MBq/cm)
Direct planes	23,870	645
Cross plane	46,880	1,267
Total	94,620	2,557
Uniform water solution (10.8 cm diameter)		
	(cps/µCi/ml)	(cps/kBq/ml)
Direct planes	517	14
Cross plane	1,025	28
Total	2,044	55

* In units of activity for pure positron emitters.

C. Count Rate

The count rate response of the system to the 108 mm flood source is shown in Fig. 3. The count rates measured with this particular source, filling about 87% of the UFOV, is a worst case for this scanner. It is estimated that the maximum trues rate and the 50% deadtime point are both in excess of 130 kcps at an activity concentration of about 140 µCi/ml. The maximum noise equivalent rate is 61 kcps at 127 µCi/ml with a random fraction of 42%. The point at which the randoms and trues rates are equal would be reached for an activity

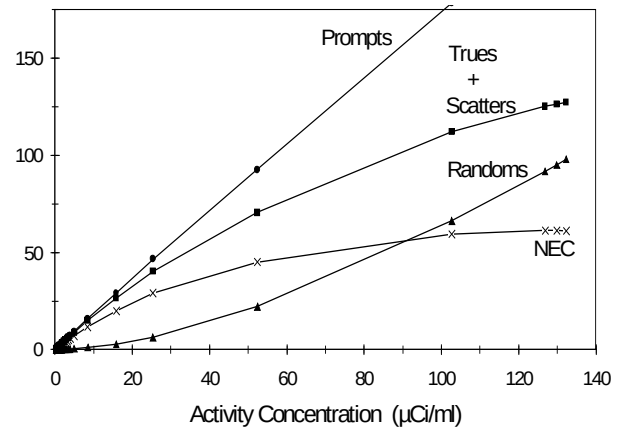

Fig. 3 - Count rate performance for a uniform 108 mm diameter cylindrical source.

concentration of the order of 175 µCi/ml. With the 20 mCi source at the center of the FOV, the trues, randoms and NEC rates were 401, 181 and 276 kcps, respectively.

D. Scatter

Object and detector scatter fractions are presented in Fig. 4 as a function of source position. The detector scatter is a characteristic of the scanner and its ratio relative to true events is independent of the object. Since the largest object which can be placed in the FOV is about 110 mm in diameter, the 16% object scatter obtained at the center is close to a maximum for this scanner. The average scatter fractions determined according to NEMA [17] are 6.3% with this object and 21.6% for the detector scatter contribution.

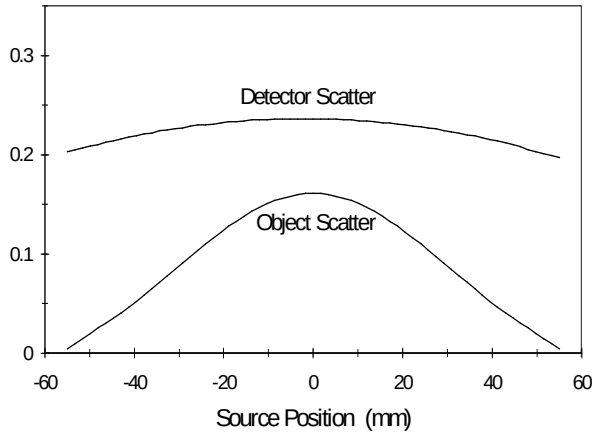

Fig. 4 - Fractions of object and detector scatter as a function of position in the field for a 110 mm diameter object and a 350 keV energy threshold.

E. Image Quality

The images of the hot and cold spot phantoms obtained without sampling motion are displayed in Fig. 5. No correction other than normalization for detector efficiency was performed on these images. The results of the contrast and recovery factor analysis are presented in Fig. 6. The contrast levels off above 80% and 50% for the hot and cold spots, respectively, mainly because corrections for randoms, scatter and attenuation were not performed. Even with these raw data, relative recovery factors better than 85% are obtained for hot and cold objects larger than 10 mm. Due to the lack of random, scatter and attenuation correction, note that the relative recovery factor should not be considered as identical to a recovery coefficient.

PET images of the ^{18}F-fluoride tracer uptake in the rat 75 minutes after injection are compared to the corresponding CT images in Fig. 7. The upper image is a coronal slice through the head around the median of the brain. The structure of the skull and lower jaw can be easily delineated in the PET image, demonstrating that the measurement of regional tracer uptake within the brain of small rats is feasible. The dome of the skull in a 160 g immature rat is

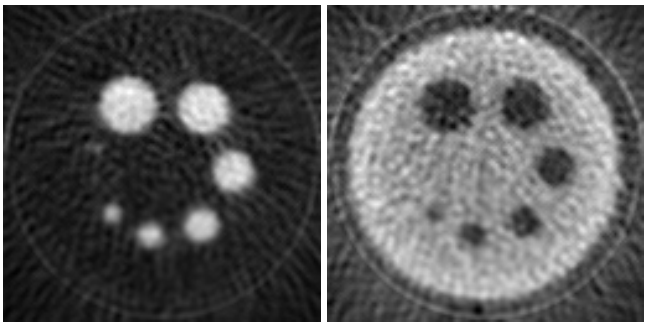

Fig. 5 - Images of hot (left) and cold (right) spot phantoms obtained without sampling motion. The acquisition time and the source activity concentration were the same for both phantoms, but the gray scale was adjusted individually to display each image.

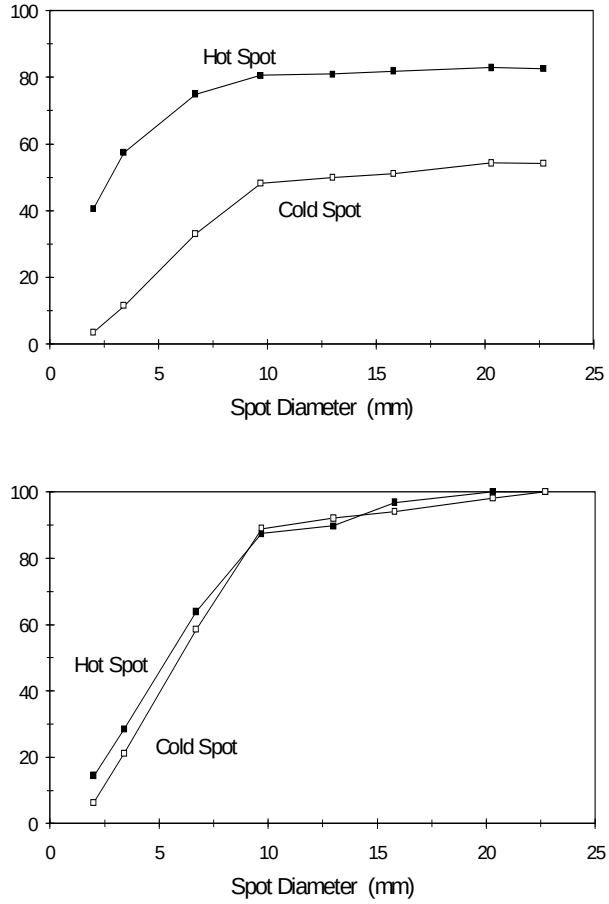

Fig. 6 - Contrast (above) and relative recovery factor (bottom) of the hot and cold spots evaluated from the images of Fig. 5.

typically much less than 1mm thick. The bottom image is a slice through the thorax at the heart level. The spine, the breastbone and the ribs are clearly visible, showing that functional cardiac studies can be considered in a rat model. The time activity curves for ROIs in that slice are plotted in Fig. 8. No correction was made for scatter and attenuation in these rat images and no attempt was made to correct for partial volume effects in the estimation of relative regional activity concentrations.

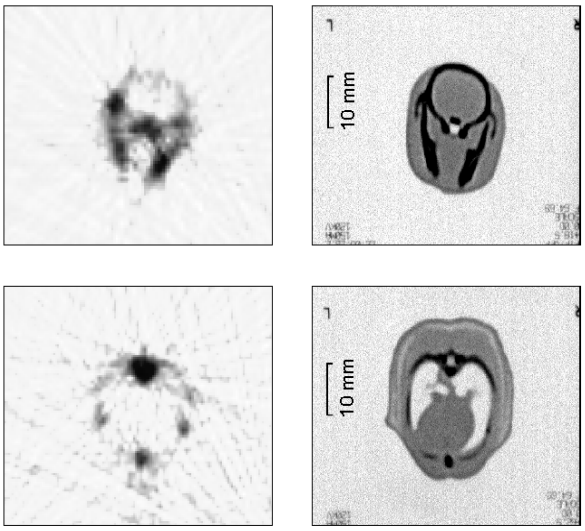

Fig. 7 - Images of the uptake of ^{18}F-fluoride in the head (above) and the thorax (bottom) of a 160 g rat obtained with the animal PET scanner (left) compared to X-ray CT images (right).

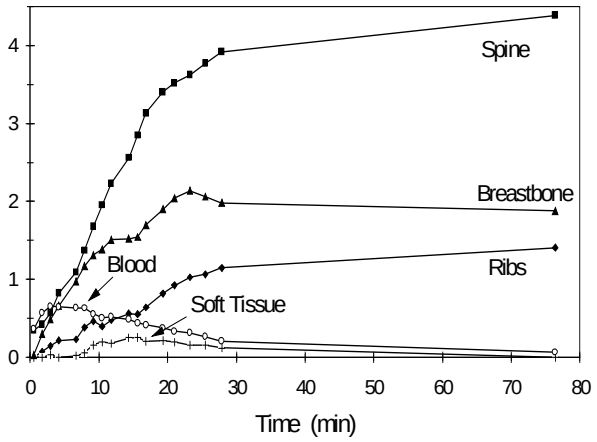

Fig. 8 - Time activity curves of ^{18}F-fluoride uptake in ROIs of the slice through the thorax shown in Fig. 7.

V. DISCUSSION

The Sherbrooke animal PET scanner is the first PET system based on APD detectors. Several specific design constraints had to be satisfied for implementing this new detector technology and for making it fully operational for imaging applications. The data presented in this paper confirm that the performance of the scanner is suitable for regional assessment of dynamic physiological parameters in small animal models. Image quality is rather insensitive to degrading factors such as nonuniform detector efficiency, scatter, randoms etc., and remains the same over large portions of the FOV.

˝ Some of the physical problems faced by the APD detectors include the poor timing resolution, the low sensitivity and the increased complexity relative to the current PMT/block detector designs. Proper tuning is critical for the spectroscopic and timing performance of every individual detector and further refinement in this area remains to be investigated. It should be noted, however, that the timing resolution does not pose a serious limitation for the performance of the scanner since the system is highly collimated and the random fraction can be kept low in most studies. The low sensitivity is a much more serious obstacle in situations where the amount of radioactivity which can be administered is limited (e.g. receptor studies, low specific activity tracers). Another major limitation at this stage is the reduced axial FOV of 10.5 mm which precludes imaging of whole organs at once. Provision has been made for expanding the axial field of the system to 50 mm with three additional detector layers.

VI. ACKNOWLEDGEMENTS

The authors wish to thank Dr. J.E. van Lier for his assistance in the animal experiments and Dr G. Schmutz for obtaining the CT scans. The contribution of EG&G Optoelectronics in supplying detectors and the financial support of the University of Sherbrooke for the supply of ^{18}F is gratefully acknowledged. This work was supported by the Medical Research Council of Canada under Grant MT-12485. The first author is a senior scholar of *Le Fonds de la Recherche en Santé du Québec*.

VII. REFERENCES

[1] M. Ingvar, L. Eriksson, G.A. Rogers et al., "Rapid feasibility studies of tracers for positron emission tomography: High-resolution PET in small animals with kinetic analysis", *J. Cereb. Blood Flow Metab.*, vol. 11, pp. 926-931, 1991.

[2] S.P. Hume, R. Myers, P.M. Bloomfield et al., "Quantitation of carbon-11-labeled raclopride in rat striatum using positron emission tomography", *Synapse*, vol. 12, pp. 47-54, 1992.

[3] R.J. Melder, A.L. Brownell, T.M. Shoup et al., "Imaging of activated natural killer cells in mice by positron emission tomography: Preferential uptake in tumors", *Cancer Res.*, vol. 53, pp. 5867-5871, 1993.

[4] C. Marriott, J.E. Cadorette, R. Lecomte et al., "High-resolution PET imaging and quantitation of pharmaceutical biodistributions in a small animal using avalanche photodiode detectors", *J. Nucl. Med.*, vol. 35, pp. 1390-1397, 1994.

[5] Y. Magata, H. Saji, S.R. Choi et al., "Noninvasive measurement of cerebral blood flow and glucose metabolic rate in the rat with high-resolution animal positron emission tomography (PET): A novel *in vivo* approach for assessing drug action in the brains of small animals", *Biol. Pharm. Bull.*, vol. 18, pp. 753-756, 1995.

[6] W.-D. Heiss, K. Wienhard, R. Graf et al., "High-resolution PET in cats: Application of a clinical camera to experimental studies", *J. Nucl. Med.*, vol. 36, pp. 493-498, 1995.

[7] M. Watanabe, H. Uchida, H. Okada et al., "A high resolution PET for animal studies", *IEEE Trans. Med. Imag.*, vol. 11, pp. 577-580, 1992.

[8] P.D. Cutler, S.R. Cherry, E.J. Hoffman et al., "Design features and performance of a PET system for animal research", *J. Nucl. Med.*, vol. 33, pp. 595-604, 1992.

[9] P.M. Bloomfield, S. Rajeswaran, T.J. Spinks et al., "The design and physical characteristics of a small animal positron emission tomograph", *Phys. Med. Biol.*, vol. 40, pp. 1105-1126, 1995.

[10] S. Tavernier, P.Bruyndonckx and Z. Shuping, "A fully 3D small PET scanner", *Phys. Med. Biol.*, vol. 37, pp. 635-643, 1992.

[11] F. Daghighian, D.M. Lovelock, B. Eshaghian et al., "Design considerations of an animal PET scanner utilizing LSO scintillators and position sensitive PMTs", *NSS & MIC 1994 IEEE Conf. Rec.*, vol. 3, pp. 1343-1346, 1994.

[12] S. Siegel, S.R. Cherry, A.R. Ricci et al., "Development of continuous detectors for a high resolution animal PET system", *IEEE Trans. Nucl. Sci.*, vol. 42, pp. 1069-1074, 1995.

[13] K. Wienhard, M. Dahlbom, L. Eriksson et al., "The ECAT EXACT HR: Performance of a new high resolution positron scanner", *J. Comput. Assist. Tomogr.*, vol. 18, pp. 110-118, 1994.

[14] R. Lecomte, J. Cadorette, P. Richard et al., "Design and engineering aspects of a high resolution positron tomograph for small animal imaging", *IEEE Trans. Nucl. Sci.*, vol. 41, pp. 1446-1452, 1994.

[15] J. Cadorette, S. Rodrigue and R. Lecomte, "Tuning of avalanche photodiode PET camera", *IEEE Trans. Nucl. Sci.*, vol. 40, pp. 1062-1066, 1993.

[16] R.H. Huesman, S.E. Derenzo and T.F. Budinger, "A two-position sampling scheme for positron emission tomography", in *Proc. 3rd World Congress of Nuclear Medicine and Biology*, ed. C. Raynaud, NY:Pergamon, 1982, pp. 542-545.

[17] J.S. Karp, M.E. Daube-Witherspoon, E.J. Hoffman et al., "Performance standards in positron emission tomography", *J. Nucl. Med.*, vol. 32, pp. 2342-2350, 1991.

[18] M. Bentourkia, P. Msaki, J. Cadorette and R. Lecomte, "Assessment of scatter components in high resolution PET: Correction by non-stationary convolution-subtraction", *J. Nucl. Med.*, vol. 36, pp. 121-130, 1995.